Bending behaviour of corroded RC continuous beams with C-FRCM strengthening system

Ran Feng[a], Panpan Liu[a], Jingzhou Zhang[b], Fangying Wang[c], Ying Xu[a], Ji-Hua Zhu[d*]

[a] *School of Civil and Environmental Engineering, Harbin Institute of Technology, Shenzhen, China (518055)*

[b] *School of Civil Engineering, Guangzhou University, Guangzhou, China (510006)*

[c] *Department of Civil Engineering, University of Nottingham, Nottingham, UK*

[d] *Guangdong Provincial Key Laboratory of Durability for Marine Civil Engineering, College of Civil and Transportation Engineering, Shenzhen University, Shenzhen, China (518060)*

Abstract

This paper presents a numerical investigation into the bending behaviour of uncorroded and corroded reinforced concrete (RC) continuous beams with a strengthening system. Finite element analysis (FEA) was performed on ten RC beams considering interface performance, including five uncorroded and five corroded beams. The cracks development, bending capacities and load-displacement curves of the simulated RC beams in the loading process were validated against those from tests. Then, a parametric study including 35 RC beam models, considering the effects of carbon-fabric (CF) mesh layer, complete wrapping layer and the degree of corrosion of steel bar on their bending capacities, was conducted. Ductility and strengthening effects of specimens were discussed in the parametric study. It can be found that the carbon-fabric reinforced cementitious matrix (C-FRCM) strengthening system can improve the bending capacities of the corroded RC beams. As the layer of CF mesh increases, the ductility of the specimen decreases. The combined use of the C-FRCM plate and the complete wrapping as the end anchorage enhanced the ultimate loads of RC beams to a greater extent than those strengthened with C-FRCM plate only. The applicability of current design codes for RC beams with C-FRCM strengthening system was examined through comparisons of the bending capacity predictions of RC beams with those obtained from tests and numerical analyses. It was found that European Code (FIB Bulletin 14) provides more accurate predictions than American Specifications (ACI 549.4R-20, AC 434-0616-R1, ACI 440.2R-17) and Chinese Code (CECS 146-2003 (2007)). Therefore, design modifications based on the most accurate design rule of FIB Bulletin 14 were made. By utilizing

*Corresponding author.
E-mail address: zhujh@szu.edu.cn (J.-H. Zhu).

regression analysis on the numerical results, the formula for bending capacities of the examined RC beams was proposed and showed improved accuracy.
Keywords: Carbon-fabric reinforced cementitious matrix (C-FRCM); Continuous beam; Corroded; Finite element analysis (FEA); Interface performance; complete wrapping

1. Introduction

The durability of reinforced concrete (RC) has always been one of the major concerns in construction, especially for offshore or coastal engineering where the RC structure is prone to long-term erosion of chloride salts [1]. The survey results of Science Press Publishing showed that in 2014, corrosion cost in China was about 2,272.8 billion RMB, accounting for 3.34% of the gross domestic product (GDP) of the year [2]. In 2003, the Research Institute of the Fourth Navigation Bureau of the Ministry of Communications investigated the damage of RC structures coastal port projects in China, indicating that more than 80% of the structures experienced severe steel corrosion damage. Extensive investigations [3-6] have documented that the corrosion of steel reinforcing bars is one of the most important factors adversely affecting the durability of RC structures.

In recent years, a considerable number of studies have focused on the fiber reinforced polymer (FRP) strengthening system, including FRP bonding behaviour and component performance. The models were given to calculate the pullout strength of FRP anchors [7-9], while the effect of the FRP anchor system on the bonding behaviour of FRP-concrete interface and the methods of improving the FRP anchor systems were analyzed [10, 11]. Refs. [12, 13] conducted a finite element analysis (FEA) of FRP-concrete joint system and showed that the anchor significantly improved the strength performance of FRP sheet. Refs. [14-17] analyzed the critical parameters that influenced the strengthening effect, which showed that the effectiveness of FRP systems and the ductility decreased with the increase of the layer of FRP. Refs. [18, 19] indicated that polyethylene terephthalate (PET)-FRP was able to improve structural performance, especially when RC structures suffered from erosion, owing to its large rupture strain and low elastic modulus. Refs. [20-23] showed that FRP can significantly improve the bending and shear capacities of the retrofitted RC beams.

In addition to the aforementioned use of FRP to solve the problem of durability, a number of recent investigations were dedicated to the static performance of RC beams strengthened with fabric

reinforced cementitious matrix (FRCM). Specifically, Refs. [24, 25] used a relatively new Near-Surface Embedded (NSE) FRCM system to examine the influence of the FRCM materials, strengthening technique, and reinforcement ratio on the structural performance of RC beams; the results showed that the hybrid NSE/EB-FRCM can be effectively used for the flexural strengthening of RC beams while carbon-fabric reinforced cementitious matrix (C-FRCM) presented a higher axial stiffness than polyparaphenylene benzobisoxazole-fabric reinforced cementitious matrix (PBO-FRCM) and glass-fabric reinforced cementitious matrix (G-FRCM). Hadad et al. [26] proposed design methods for RC beams strengthened by FRCM, where the relationship between the FRCM reinforcement ratios and the ultimate capacities of RC beams was established. Refs. [27, 28] discussed the influences of parameters on flexural performance of RC continuous beams strengthened with FRCM system, including the type of the strengthening system, the strengthening location and the layer of the FRCM. It revealed that RC beam strengthened with FRCM system had perfect rotational capacity and efficient redistributed moments between their critical sections. Wakjira et al. [29] presented a data-driven approach to determine the bending capacities of RC beams strengthened with FRCM, which had superior predictive capability and robustness. Su et al. [30] introduced the technique of the combined ICCP-SS for repairing RC structures subjected to chloride-induced corrosion. The development of this technique was based on the combination of a carbon-fabric (CF) mesh and a polymer-modified cementitious matrix to produce a C-FRCM system. Zhu et al. [31] carried out an experimental program on ten stub columns, and results showed that the proposed ICCP-SS technique was not only effective in retarding the corrosion of steel bars but also capable of recovering the compression capacities of the corroded RC columns.

Previous investigations into RC beams strengthened by FRP or FRCM have been focused on simply-supported beam configuration, while the present study explored the C-FRCM plate strengthened continuous beams considering the fact that, continuous beam is also widely adopted in practical RC structures and also differs from simply-supported beam by moment redistribution. In general, more attention has been paid to the structural performance, mainly the failure modes and strengthening effectiveness. Meanwhile, the existing design methods have not been comprehensively summarized except those from American Specifications. To date, there have been rather limited research using numerical simulation to predict the failure modes and crack development; therefore this is the focus of the present study. In order to reflect the real cases in

constructions, this study examined continuous beam specimens numerically. Finite element models (FEMs) were first established and validated with experimental data in the literature and then used to conduct an extensive parametric study. It was noticed from previous experimental studies that the failure generally occurred between CF mesh and cementitious matrix, and in some cases, between concrete and cementitious matrix. Therefore, the definition and simulation of the interface between the aforementioned components are essential to reproduce the test failure modes, and influence the ultimate capacities. However, these interface simulations have not been thoroughly considered in the existing FE studies on RC structures [32-36].

In this study, all the critical interfaces were simulated at the first attempts, including the interface between CF mesh and cementitious matrix, the interface between C-FRCM plate and concrete, and the interface between U-shaped wrapping and beam, utilising finite element program DIANA. The development of cracks, ultimate loads, bending capacities, and load-displacement curves were validated against experimental results, and discussions were conducted on the ductility and strengthening effect of specimens. The effects of the CF mesh layer, complete wrapping layer and the degree of corrosion of steel bar on the bending capacities of RC beams were investigated in a parametric study. Then, the suitability of the current design codes for determining the bending capacities of RC beams with C-FRCM strengthening system was evaluated. Finally, the formula for bending capacities of RC beams with the C-FRCM strengthening system was proposed based on the test results, numerical results and code calculations, which was validated to be accurate.

2. A brief summary of experimental work

An experimental programme was carried out by the authors to investigate the behaviour of RC beams strengthened by C-FRCM. A brief summary is introduced herein, and a full description of the tests is provided in Ref. [37]. A total of ten (five uncorroded and five corroded beams) RC two equal-span continuous beams with the same cross-section dimensions and reinforcement ratios were tested to investigate the bending capacities of C-FRCM strengthened RC continuous beams. The total length of the beam is 2400 mm, and the cross-section dimension is 150×250 mm. The details of the dimensions, boundary conditions and steel bars of the specimens are shown in Fig. 1. The diameter of the longitudinal steel bars is 10 mm located at the top and the bottom of RC beam; the diameter of the stirrups is 8 mm with a space of 80 mm. One support is located at the mid-span of

beam, and the remaining two supports are located 100 mm away from the beam ends. According to the CF mesh layer, complete wrapping layer and the degree of corrosion of the steel bar, the details of the specimens are summarized in Table 1. The specimen identification system (e.g. B-L0-U0) starts with the letter 'B' symbolizing an uncorroded beam ('CB' indicating a corroded beam), followed by 'L' with a number representing the layers of C-FRCM, and ends with 'U' with a number designating the layers of complete wrapping. The material properties including the degrees of corrosion of steel bars in corroded specimens are shown in Table 2. The arrangement of the C-FRCM plates and the complete wrappings is presented in Fig. 2. The C-FRCM plates are located in the regions with relatively large bending moments and the complete wrappings are placed 115 mm away from both ends of the C-FRCM plate. The test setup of static bending tests of RC beams is displayed in Fig. 3 and the experimental results, including the failure modes and bending capacities, are detailed in Ref. [37].

3. Finite element modelling

A nonlinear finite element program called DIANA (Displacement Analyzer) [38] was used in this study to conduct a 3D nonlinear analysis of the specimens. DIANA [38] is capable of accurately simulating the whole process of the RC structures from the initial state, cracking, the development of cracks to the final structure damage. In the simulation process, the actual geometry of the structure, the material properties of concrete and the crack constitutive relationship, and the material properties of steel bar, CF mesh, cementitious matrix were considered.

In the current study, a total of ten FEMs, including one unstrengthened uncorroded beam, four strengthened uncorroded beams, one unstrengthened corroded beam, and four strengthened corroded beams were established and analyzed with DIANA using Regular Newton Raphson method [38].

3.1. Material properties

3.1.1. Concrete

For modelling concrete material in the examined RC beams, particular attention was put on the crack simulation of the concrete, which is deemed to significantly affect the structural performance of RC beams. The smear crack model, known to be capable of simulating the development of cracks

of concrete, was adopted. In general, the smeared crack model treats the crack as a directional distribution effect, and the cracked material is then simulated as a continuous medium with anisotropic characteristics. Among the smeared crack model categories, a total strain crack model based on total strain was established based on the modified strain field theory, which was originally proposed by Vecchio and Collins [39], and further employed by Selby and Vecchio [40] to extend the theory in three dimensions. The 'Fixed Crack Model' with 'fixed cracking' for the tension behaviour, as one of the total strain crack model categories, has been widely used [41-43] and was adopted for concrete herein. In the fixed crack model, the crack orientation is saved as a status parameter, which is defined as the direction of the maximum principal strain corresponding to the tensile strength. The main stress-strain conditions are evaluated in an orthogonal coordinate system that aligns the coordinates with the principal strain at the time of the first crack [38].

The main properties of concrete in the total strain crack model were defined as follows:

Regarding concrete tensile properties, it is assumed that the concrete is linear elastic before cracking:

$$\sigma_t^{ef} = E_c \varepsilon^{eq} \tag{1}$$

where σ_t^{ef} is the effective tensile stress of concrete, ε^{eq} is the effective uniaxial tensile strain, and E_c is the initial elastic modulus of concrete.

The crack opening rule proposed by Hordijk [44] was adopted as the constitutive relationship of concrete after cracking herein. The simplified diagram is shown in Fig. 4a, and the crack opening function is as follows:

$$\frac{\sigma}{f_t^{'ef}} = \left\{1+\left(c_1\frac{w}{w_c}\right)^3\right\} exp\left(-c_2\frac{w}{w_c}\right) - \frac{w}{w_c}\left(1+c_1^3\right) exp\left(-c_2\right) \tag{2}$$

$$w_c = 5.14\frac{G_f}{f_t^{'ef}} \tag{3}$$

where w is the crack opening displacement, w_c is the crack opening displacement when the stress is fully released, σ is the normal stress in the crack direction, constant c_1 is equal to 3, c_2 is equal to 6.93, G_f is the tensile fracture energy, and $f_t^{'ef}$ is the effective tensile strength of concrete.

The crack opening displacement (w) can be obtained according to the crack zone theory proposed by Bazant and Oh [45]:

$$w = \varepsilon_1 L_t^{'} \tag{4}$$

where ε_1 is the crack opening strain perpendicular to the direction of the crack after the cracking stress is completely released, and $L_t^{'}$ is the length of the failure zone in tension.

Concrete subjected to compressive stresses shows a pressure-dependent behaviour, indicating that the strength and ductility increase with the increase of isotropic stress. In this study, the compressive stress-strain relationship in DIANA [38] was represented by a predefined parabolic function, which is based on the formulas derived from the fracture energy [46], as shown in Fig. 4b. The parabolic curve is described by the strain corresponding to a certain compressive strength (α_j) dependent on three characteristic parameters, the strain when one-third of the maximum compressive strength is reached ($\alpha_{c/3}$), the strain corresponding to the ultimate compressive strength (α_c) and the strain at which the material is completely softened (α_u), which can be obtained from Eqs. 5-7, respectively.

$$\alpha_{c/3} = -\frac{1}{3}\frac{f_c}{E_c} \tag{5}$$

$$\alpha_c = -\frac{5}{3}\frac{f_c}{E_c} = 5\alpha_{c/3} \tag{6}$$

$$\alpha_u = min\left(\alpha_c - \frac{3}{2}\frac{G_c}{h_l f_c}, 2.5\alpha_c\right) \tag{7}$$

The parabolic compression curve in DIANA [38] can be expressed by the functions in Eq. 8. It reveals the compressive fracture energy (G_c) and the characteristic element length (h_l) only control the softening part of the curve, as also indicated mathematically from Eq. 9.

$$f = \begin{cases} -f_c \dfrac{1}{3}\dfrac{\alpha_j}{\alpha_{c/3}} & \text{if } \alpha_{c/3} < \alpha_j \le 0 \\ -f_c \dfrac{1}{3}\left(1 + 4\left(\dfrac{\alpha_j - \alpha_{c/3}}{\alpha_c - \alpha_{c/3}}\right) - 2\left(\dfrac{\alpha_j - \alpha_{c/3}}{\alpha_c - \alpha_{c/3}}\right)^2\right) & \text{if } \alpha_c < \alpha_j \le \alpha_{c/3} \\ -f_c\left(1 - \left(\dfrac{\alpha_j - \alpha_c}{\alpha_u - \alpha_c}\right)^2\right) & \text{if } \alpha_u < \alpha_j \le \alpha_c \\ 0 & \text{if } \alpha_j \le \alpha_u \end{cases} \tag{8}$$

$$\int_{\alpha_c}^{\alpha_u} f \, d\alpha_j = f_c\left(\alpha_j - \frac{1}{3}\frac{\left(\alpha_j - \alpha_c\right)^3}{\left(\alpha_u - \alpha_c\right)^2}\right)\Bigg|_{\alpha_c}^{\alpha_u} = \frac{G_c}{h_l} \tag{9}$$

It is worth noting that the concrete material test can only provide the cubic compressive

strength value (f_{cu}), however, the concrete constitutive theory requires the axial compressive strength (f_c) and tensile strength (f_t) in the simulation process. Therefore, the axial tensile strength (f_t) was calculated as 2.01 MPa and the elastic modulus (E_c) was set as 30 GPa, according to Chinese Code (GB 50010-2010) [47]. Moreover, the cubic compressive strength of concrete was converted into the axial compressive strength (f_c), as shown in Eq. 10, where α_{c1} is the strength convert ratio, taken as 0.76 herein, and α_{c2} is the brittleness reduction coefficient for high strength concrete, taken as 1.00 in this study.

$$f_c = 0.88 \times \alpha_{c1} \times \alpha_{c2} \times f_{cu} \tag{10}$$

The concrete strength and elastic modulus of corroded specimens were assumed not to be deteriorated due to the limited time of the natural corrosion for the specimens. The concrete material properties used in the simulation are summarized in Table 2.

3.1.2. Steel bar

The longitudinal steel bar and the stirrup were simulated by using the double slash constitutive model, in which the steel materials are characterized by Von Mises yield criterion with isotropic strain hardening. The material properties of steel bars under different degrees of corrosion were converted from those of uncorroded specimens, following the conversion formulas in Wu and Yuan [48], as presented in Eqs. 11 and 12,

When $0 < \rho\% \leq 5\%$,

$$\begin{aligned} f_{yc} &= f_{y0}\left(1 - 0.029\rho\right) \\ f_{uc} &= f_{u0}\left(1 - 0.026\rho\right) \\ \varepsilon_{yc} &= \varepsilon_{y0}\left(1 - 0.0575\rho\right) \\ E_{uc} &= E_{u0}\left(1 - 0.052\rho\right) \end{aligned} \tag{11}$$

When $\rho\% > 5\%$,

$$\begin{aligned} f_{yc} &= f_{y0}\left(1.175 - 0.064\rho\right) \\ f_{uc} &= f_{u0}\left(1.18 - 0.062\rho\right) \\ \varepsilon_{yc} &= \varepsilon_{y0}\left(1 - 0.0575\rho\right) \\ E_{uc} &= E_{u0}\left(0.895 - 0.031\rho\right) \end{aligned} \tag{12}$$

where $\rho\%$, E_{uc}, f_{yc}, f_{uc} and ε_{sc} are the degree of corrosion, elastic modulus, yield strength, ultimate strength and ultimate strain of corroded steel bars, respectively, while E_{u0}, f_{y0}, f_{u0} and ε_{s0} correspond

to those properties of the uncorroded steel bars.

The bonding behaviour between steel bar and concrete was also considered [49, 50]. For uncorroded specimens, the bond-slip constitutive model of steel bar in the CEB-FIP Code [50] was adopted, and the theoretical equations are presented in Eq. 13,

$$\begin{aligned} \tau &= \tau_{max}\left(\frac{s}{s_1}\right)^{\alpha} && 0 \le s \le s_1 \\ \tau &= \tau_{max} && s_1 < s \le s_2 \\ \tau &= \tau_{max} - \left(\tau_{max} - \tau_f\right)\left(\frac{s - s_2}{s_3 - s_2}\right) && s_2 < s \le s_3 \\ \tau &= \tau_f && s_3 < s \end{aligned} \tag{13}$$

where τ is the local bonding strength, τ_{max} is the maximum local bonding strength, s is the local slip, α is the slip coefficient, set as 0.4, and s_1, s_2 and s_3 are the critical slip parameters, taken as 0.6, 0.6 and 1.0, respectively, as shown in Table 3.

For the bond-slip behaviour of corroded steel bars and concrete, the bonding strength τ_c is factored by a correction coefficient (β), which was proposed by Xu [51] for considering the reduced bonding after corrosion, as given by Eq. 14.

$$\beta = \begin{cases} 1 + 0.5625\rho - 0.3375\rho^2 + 0.55625\rho^3 - 0.003\rho^4 & \rho\% \le 7\% \\ 2.0786\rho^{-1.0369} & \rho\% > 7\% \end{cases} \tag{14}$$

3.1.3. CF mesh and CFRP complete wrapping

The CF mesh setting adopted in this study is visualized in Fig. 5, where the transverse and the longitudinal fiber widths are 2 and 5 mm, respectively, spaced at 10 mm in both orthogonal directions. In the simulation, it is assumed that the nodes of the transverse and longitudinal fibers are in good contact, and the CF mesh is a linear elastic material. The reinforcing mesh element in DIANA [38] can be used to simulate the bidirectional CF mesh, however not the bond-slip behaviour. Therefore, the CF mesh was simplified to be the membrane with the thickness of 0.1 mm in order to consider the interface behaviour. The CF mesh membrane adopted a linear elastic constitutive relationship with the elastic modulus (E_t) of 132 GPa, the maximum tensile strength (f_{tu}) of 1350 MPa, and the ultimate tensile strain (ε_{tu}) of 1.15%. The CFRP complete wrapping is unidirectional FRP, which was simulated using a linear elastic isotropic model [52, 53] with the Poisson's ratio of 0.2 and the modulus of elasticity (E_{frp}) of 240 GPa.

3.1.4. Cementitious matrix

The cementitious matrix adopted the identical compressive and tensile constitutive relationships as those of concrete. The elastic modulus of concrete was also utilized for the cementitious matrix. The ultimate tensile strength of cementitious matrix (f_{cmt}) was obtained based on the corresponding ultimate compressive strength (f_{cmc}) according to ACI 318 [54], as given by Eq. 15.

$$f_{cmt} = 0.62\sqrt{f_{cmc}} \tag{15}$$

3.2. Modelling of interface performance

3.2.1. Modelling of the interface between CF mesh and cementitious matrix

The nonlinear elastic interface element in DIANA [38] was selected to simulate the interface behaviour between CF mesh and cementitious matrix. The CF mesh was assigned as the source surface, while the cementitious matrix was chosen as the target surface. The trilinear bond-slip relationship for the carbon yarn-matrix interface given in Ref. [55] (as shown in Fig. 6a) was adopted in this study, which is divided into three segments: elastic, debonding, friction, along with four key parameters such as the slope of the elastic segment (k_1), the slope of the debonding segment (k_2), maximum bonding stress between carbon yarn and cementitious matrix ($\tau_{max,cf}$), bonding stress during friction segment ($\tau_{0,cf}$) are included.

In the elastic segment, the relation between applied load in pullout test (P) and pullout displacement (u) is given as follows:

$$P = E_{cf} A_{cf} \lambda_1 \tanh(\lambda_1 L) u \tag{16}$$

where E_{cf} is the Young's modulus of carbon yarn obtained from axial tensile test, A_{cf} is the cross-sectional area of carbon yarn, and L is the bonding length of carbon yarn, respectively.

The relationship between the temporary variable of the elastic segment (λ_1) and k_1 is given in Eq. 17.

$$\lambda_1 = \sqrt{\frac{c_{cf} k_1}{EA}} \tag{17}$$

where c_{cf} is the perimeter of a single carbon yarn.

In the debonding segment, the relation between P and u is expressed as:

$$P = EA\lambda_2 \tan(\lambda_2 L)\left(\frac{k_1 + k_2}{k_1 k_2}\tau_{max,cf} - u\right) \quad (18)$$

The relationship between the temporary variable of the debonding segment (λ_2) and k_2 is given in Eq. 19.

$$\lambda_2 = \sqrt{\frac{c_{cf} k_2}{EA}} \quad (19)$$

In the friction segment, the $\tau_{0,cf}$ is as given by Eq. 20:

$$\tau_{0,cf} = \frac{P_0}{cL} \quad (20)$$

where P_0 is applied test load corresponding to the point where the last branch of bond-slip relationship.

3.2.2. Modelling of the interface between C-FRCM plate and concrete

The bond-slip interaction at the interface between the C-FRCM plate and concrete beam, which has not been considered in previous numerical investigations [32, 33, 35, 36], was considered herein to obtain the mechanical behaviour of the RC beams more accurately. The interface between the C-FRCM plate and the concrete is essentially the interface between the cementitious matrix and the concrete. Considering a lack of experimental data on the interface performance of the cementitious matrix and concrete, that of engineered cementitious composites (ECC) and concrete interface in Ref. [56] was attempted herein. Therefore, the bond-slip interaction is defined by the shear strength of ECC to concrete interface (τ_{cm}) and the interface slip (s_{cm}), as given by Eq. 21.

$$\tau_{cm} = \begin{cases} \tau_{cmu}\dfrac{s_{cm}}{s_{cm0}} & 0 \le s_{cm} \le s_{cm0} \\ \tau_{cmu}\dfrac{s_{cmu} - s_{cm}}{s_{cmu} - s_{cm0}} & s_{cm0} \le s_{cm} \le s_{cmu} \end{cases} \quad (21)$$

where τ_{cmu} is the ultimate shear strength of ECC-to-concrete interface, s_{cm0} is the interface slip corresponding to the ultimate shear strength, and s_{cmu} is the ultimate interface slip. These parameters were found to be directly linked with the uniaxial compressive strength of ECC (σ_{cm}) and the interface roughness value (χ), and can be calculated by Eqs. 22-24 given in Ref. [56].

$$\tau_{cmu} = \sigma_{cm}\left(a \times e^{\chi/b} + c\right) \quad (22)$$

$$s_{cm0} = \left(-0.013e^{\chi/-0.89} + 0.016\right)\sigma_{cm} + \left(-29310.74e^{\chi/1084419.4} + 29310.8\right) \quad (23)$$

$$s_{cmu} = \left(0.0044e^{\chi/-0.99} + 0.0092\right)\sigma_{cm} + \left(-0.76e^{\chi/-0.82} + 0.44\right) \quad (24)$$

where *a*, *b* and *c* are the fitting parameters, and summarized in Table 4 for various roughness. It was found in the experiments that the interface between cementitious matrix and concrete is relatively weak. Hence, the set of constitutive data with the smallest cohesive force was used and the constitutive relationship of the interface between cementitious matrix and concrete is shown in Fig. 6b.

3.2.3. Modelling of the interface between complete wrapping and beam

For the interface between the complete wrapping and the RC beam, the numerical analysis employed the constitutive model in Lu et al. [57], which has been widely used and deemed suitable for FRP strengthening RC members using epoxy resin. Lu et al. [57] suggested the use of a segmented interface slip relationship, as given by Eq. 25.

$$\tau_u = \begin{cases} \tau_{u\max}\left(\sqrt{\dfrac{s_u}{s_{u0}A} + B^2} - B\right) & s_u \le s_{u0} \\ \tau_{u\max} e^{-\alpha\left(\frac{s_u}{s_{u0}} - 1\right)} & s_u > s_{u0} \end{cases} \quad (25)$$

where $A = \left(s_{u0} - s_{ue}\right)/s_{u0}$, $B = s_{ue}/\left[2\left(s_{u0} - s_{ue}\right)\right]$ and s_{ue} is the elastic part of the slippage (s_{u0}) at the interface between the complete wrapping and the beam. The relationship between τ_{umax}, s_{u0} and f_t can be obtained from Eqs. 26 and 27 given in Ref. [57].

$$\tau_{u\max} = \alpha_{u1}\beta_w f_t = \alpha_{u1}\sqrt{\frac{2.25 - b_f/b_c}{1.25 + b_f/b_c}} f_t \quad (26)$$

$$s_{u0} = \alpha_{u2}\beta_w f_t + s_{ue} = \alpha_{u2}\beta_w f_t + \tau_{u\max}/K_0 \quad (27)$$

where β_w is the width influence coefficient of FRP-to-concrete, b_f/b_c is the width ratio, and K_0 is the initial stiffness of the bond-slip relationship, which is the series stiffness including the adhesive layer shear stiffness and the concrete substrate shear stiffness, as given by Eq. 28.

$$K_0 = K_a K_c / \left(K_a + K_c\right) \quad (28)$$

where K_a is the shear stiffness of the adhesive layer and equal to G_a/t_a, in which G_a and t_a are the elastic shear modulus and thickness of the adhesive layer involved in the shear, respectively, K_c is the shear stiffness of the concrete substrate involved in the shear deformation and taken as G_{ck}/t_c, in which G_{ck} is the elastic shear modulus of the concrete, and t_c is the effective thickness of the

concrete substrate participating in the shear deformation, taken as 5 mm according to the meso-level FEA [57]. According to the meso-level FEA results, the total interface failure energy (G_{uf}) can be expressed as:

$$G_{uf} = \alpha_{u3}\beta_w^2\sqrt{f_t}\, f(K_a) \tag{29}$$

where $f(K_a)$=1 is for ordinary adhesive layer. The values of a_{u1}, a_{u2} and a_{u3} were suggested to be 1.50, 0.0195 and 0.308, respectively [57]. Finally, the obtained bond-slip constitutive relationship of the interface between the complete wrapping and beam is displayed in Fig. 6c.

3.3. Element type and mesh size

The element type in DIANA [38] is not arbitrarily specified, but is determined by the software according to the shape of the part and the mesh accuracy required by the user. The CHX60 element was selected for concrete and cementitious matrix due to its computational advantage, which is a twenty-node isoparametric solid brick element based on quadratic interpolation and Gauss integration. In order to facilitate numerical simulation, the coupling was set to convert the distributed load into the concentrated load, so the tetrahedral CTE30 and pyramid CPY39 elements were used at the loading point of the cushion block, and CHX60 element was still selected at the edge of the cushion block (see Fig. 7). The CQ24GM element, which is a 3D membrane element with 8 nodes, was selected for CF mesh and complete wrapping for more accurate simulation.

Prior to the parametric study, a sensitivity study of mesh size was conducted. Three mesh sizes of 20, 30 and 40 mm were utilized for the beam model to examine the effect of mesh size on the FEA results. The results are presented in Table 5, where the accuracy and efficiency of the numerical analyses are compared for the specimen B-L2-U3 with different mesh sizes. From the comparisons, a mesh size of 30 mm was chosen for the numerical analyses, as it achieved an acceptable accuracy while retaining the computational efficiency.

3.4. Loading and boundary conditions

In DIANA [38], it is necessary to set constraints on the coupling points and restrict the horizontal, vertical, and out-of-plane displacements when a displacement-controlled loading system is adopted for the coupling point. The vertical and out-of-plane displacements are constrained at supports of the west (W) side and the east (E) side of the beam, while the horizontal, vertical and

Commented [FW(1]: Dangling modifier!!! (the coupling 不是 facilitate numerical simulation 的动作发出者）应该可以这样写：In order to facilitate numerical simulation, ... (避免了悬垂结构的使用）

out-of-plane displacements are constrained at the mid-support of the beam. These settings mirrored the boundary condition in the experiments.

4. Validation of FEMs

4.1. General

Upon establishing the models in DIANA [38], the FEA results, such as crack strain development, ultimate load and load-displacement curve, were obtained and compared with the test results in the literature [37], as detailed in the following subsections.

4.2. Comparison of failure modes

The test failure modes of continuous beams are compared with results from numerical analyses, as shown in Fig. 8. It can be observed that the locations of the cracks of concrete are in good agreement with those of the tests, which indicates that FEA can effectively predict the crack development of the test beams. Specifically, the crack of concrete and fracture of C-FRCM plate is captured by FEA, as shown in Figs. 8a and 8b, respectively. The failure of complete wrapping and delamination of C-RFCM from the concrete substrate is revealed by the corresponding interface performance, as shown in Figs. 8c and 8d, respectively. It can be concluded that once the interface bond reaches the maximum value, the corresponding interface fails.

4.3. Comparison of bending capacities

Table 6 shows the comparison of the ultimate loads between test and FEA results. It is evident that the test results (P_{ut}) are in great agreement with the FEA results (P_{uf}), with the mean ratio of P_{ut}/P_{uf} equal to 0.99 and the coefficient of variation (COV) of 0.037. Moreover, the ultimate bending moments obtained from the tests (M_{ut}) are in line with those determined by the FEA (M_{uf}), achieving a mean ratio M_{ut}/M_{uf} of 1.07 and a COV of 0.059.

The comparisons of load-displacement curves are presented in Fig. 9. The specimens B-L0-U0 and CB-L0-U0 are set as the benchmark models of the strengthened uncorroded and strengthened corroded RC beams, respectively. The disparities between P_{uf} and P_{ut} of the specimens B-L0-U0 and CB-L0-U0 are only 0.99% and 1.00%, respectively. For the specimens B-L2-U0 and B-L3-U0, the ultimate loads of FEA are consistent with the test results, and the differences between the

simulated ultimate loads and the experimental ultimate loads of the specimens B-L2-U0 and B-L3-U0 are only 1.00% and 5.00%, respectively. The shapes of the numerical load-displacement curves are generally consistent with the testing curves. After reaching the peak, the numerical curve and the testing curve levelled off with no obvious descending part. For the specimen B-L2-U3, the differences are only 1.00% and the numerical curves are in good agreement with the testing curves. However, the failure of RC continuous beam in the tests occurred in one span, the displacement gap between the two spans in the test gradually increased with the applied loads, which cannot be replicated under symmetrical loading in FEA. For the specimen CB-L2-U0, the difference between the simulated ultimate capacity and the experimental ultimate capacity is 7.00%. However, the overall numerical curve appears to be rather different from those from the tests for the initial stage, while the differences were significantly reduced once the displacement exceeded 3 mm. This is believed that the differences at the initial stiffness were essentially owing to the inaccuracy of experimental results, which might be triggered by the inevitable human errors in the test. For the specimen CB-L3-U0, the initial stiffnesses of the numerical and experimental curves are close, yet the peak value of the numerical curve is higher than that of test curve by approximately 8%. For the specimen CB-L3-U2, the difference in ultimate loads is only 2.00%, while the development of the full load-displacement curve can be simulated well, but the descending stage of the numerical curve is slightly different from the test results. It is owing to the reason that a linear elastic material constitutive relationship of the complete wrapping was used in the numerical analyses for simplicity, therefore the sharp drop of the curves due to the failure of the material beyond the peak load in the test cannot be simulated by the numerical analyses.

Generally speaking, it was found in Fig. 9 that, for some specimens, the FE curves differed greatly from the experimental counterparts. The primary reason attributed to the large discrepancy is the fact that the experimental results involved unintentional human error and inconsistency in the corroded RC continuous beam. In the experiments, one span always failed first, however, in FE simulation, both spans failed simultaneously. This can be observed from Fig. 9 that, FE curves are identical for both west side span and east side span, whist, test curves on both spans showed great difference. Overall, it was found that the FE curves generally matched well with one of the test curve from the two spans.

5. Parametric study

5.1. General

In this study, two key structural parameters were investigated, i.e., the layer of C-FRCM plate and complete wrapping and the degree of corrosion of steel bar. It was found that the layer of CF mesh has a great influence on the ultimate load of beam according to Feng et al. [37]. Extensive studies [3-7] have also shown that the degree of corrosion of steel bar has an impact on the ultimate load and force mechanism of RC beams. Therefore, these two parameters, together with the layer of complete wrapping, were selected as the variables herein.

The parametric study comprising 35 numerical models was carried out. The models employed the same mesh size and boundary conditions as the benchmark validated models, and also considered the interface performance. The specific parameters, the ultimate loads (P_{uf}) and ultimate bending moments (M_u) of the validated numerical models and parametric models are presented in Table 7, where i_1, i_2, i_3, i_4 and i_5 as suffix in the labelling system represent the corrosion degree of 2%, 4%, 6%, 8% and 10%, respectively.

5.2. Ductility analysis

The ductility of the RC beams was investigated by comparing the ductility index (δ_u), as defined by Eq. 30,

$$\delta_u = \frac{u_u}{u_y} \tag{30}$$

where u_u represents the displacement corresponding to the ultimate load, and u_y represents the displacement at which the longitudinal bar starts to yield, yield strain of longitudinal bars can be captured by the strain gauges embedded at longitudinal bars of RC beams.

Typical comparisons of the ductility index are illustrated in Fig. 10. The effects of CF mesh layers on the uncorroded and corroded specimens are shown in Figs. 10a and 10b, respectively. The values of δ_u for uncorroded beams are found to be 4.56%, 4.59% and 3.08% for B-L1-U0, B-L2-U0, and B-L3-U0, respectively, which are 28.3-51.6% lower than the unstrengthened uncorroded beam (B-L0-U0) and the ductility retention reaches 71.7%-72.2% of that of specimen B-L0-U0. While values of δ_u for corroded beams are 3.41%, 3.21% and 2.43% for specimens CB-L1-U0, CB-L2-U0, and CB-L3-U0, respectively, which are 26.3-47.5% lower than the unstrengthened corroded beam (CB-L0-U0) and still 69.3-73.7% of the ductility relative to the specimen CB-L0-U0 is retained. It

is evident that the ductility of the specimens decreases significantly with the increase of the CF mesh layers from none to one and from two to three, however, less so for the layers change from one to two. The trend is consistent with Ref. [58] using the same mix proportion of C-FRCM, where the values of δ_u are 4.78% for the strengthened uncorroded beam with one-layer CF mesh and 4.75% for the strengthened uncorroded beam with two-layer CF mesh.

The influence of the corrosion degree of steel bar is shown in Fig. 10c. It can be seen that the ductility of the specimens (CB-L3-U0 series) strengthened with three-layer C-FRCM plates is 11.6-48.7% lower than that of the RC beams (CB-L2-U0 series) strengthened with two-layer C-FRCM plates. Yet, the ductility index of the component will increase slightly with the increase of corrosion degree, owing to the reduction of the corresponding displacement when the steel bar yields (i.e., u_y is reduced). Furthermore, the ductility of the member strengthened with C-FRCM is not weakened by the corrosion of the longitudinal bars, which explains the superiority of the C-FRCM strengthening system. The ductility comparison of specimens with different layers of complete wrappings is shown in Fig. 10d. Compared with strengthened beams with one layer of complete wrapping, ductility increases by no more than 2.3% (for B-L1 series), 16% (for B-L2 series) and 3.0% (for B-L3 series), respectively. It can be seen that the layer of complete wrapping, compared to the layer of CF mesh, appears to be less influential to the ductility of the RC beam.

Overall, it can be concluded that the ductility of RC beam retained well with one or two layers of C-FRCM plate was not affected by the corrosion degree of specimens strengthened with C-FRCM plates, indicating that the C-FRCM strengthening system is feasible for corroded RC specimens.

5.3. Strengthening effect

The strengthening effect (i.e. of C-FRCM strengthened RC beams is discussed in Fig. 11, where the increased strengths are normalized by the strength of the specimen B-L0-U0. The parameters investigated herein are the layer of CF mesh, with or without complete wrapping, the layer of complete wrapping, and the corrosion degree of steel bar, as shown in Figs. 11a-11d. It can be seen from Fig. 11a that the values of the strengthening effect of specimens B-L1-U0, B-L2-U0 and B-L3-U0 considering the influence of the layer of CF mesh are 1.13%, 4.97%, 10.74%, respectively, while those of simply-supported beams S-B-L1 and S-B-L2 are 1.34%, 6.73%, respectively, as per [58]; indicating that the strengthening effect of two layers of CF mesh is over

4.40 times of the strengthening effect of one layer of CF mesh and the layer of CF mesh has a crucial impact on the strengthening effect. Fig. 11b shows the strengthening effect of three series, CB-L1 series (CB-L1-U0 and CB-L1-U3), CB-L2 series (CB-L2-U0 and CB-L2-U3) and CB-L3 series (CB-L3-U0 and CB-L3-U3), are 1.13%, 1.93, 4.97%, 8.26%, 10.74%, 11.34%, respectively; demonstrating that the use of three-layer complete wrapping has a considerable impact on the strengthening effect, but the difference in strengthening effect is less than 3.29%. Fig. 11c displays two opposing trends as the number of complete wrapping layers increases; for specimens with two layers of CF mesh, the values of strengthening effect of two layers of CF mesh are 5.19%, 7.58%, 8.26%, respectively, showing slightly increase with the use of more layers of complete wrapping. However, decreased from 14.03% to 11.34% for specimens with three layers of CF mesh. This might be owing to the reason that the overuse of complete wrappings cannot effectively exert the strengthening effect, and adversely influence the strength performance of RC specimens. The results with respect to anchorage systems are not conclusive, further research is needed to further understand the influences of anchorage systems [59], yet that the use of anchorage systems to impede the FRCM debonding and enhance the flexural performance of the strengthened beams was fully recognised [60-62]. Fig. 11d shows evidently that corrosion degree of steel bar reduced on the strengthening effect of the specimen, however, this can be slightly compensated by the increased number of CF mesh layers.

Based on the discussion about Sections 5.2 and 5.3, it can be seen that the ductility of the two-layer CF mesh is basically the same as that of the one-layer CF mesh while that of the three-layer is the poorest. But the strengthening effect of three-layer CF mesh is better than that of one-layer and two-layer CF mesh. Moreover, debonding phenomenon is effectively prevented with the increase of ductility using complete wrappings. In order to ensure sufficient ductility of the component, it is recommended to adopt the two-layer CF mesh with three-layer complete wrappings to prevent debonding and obtain enough ductility.

Commented [FW(2]: + the (最高级）

6. Design guidelines

6.1. General

Currently, there is no design code available for corroded RC continuous beam with C-FRCM strengthening system. Therefore, to predict the bending capacity of corroded RC continuous beam

with C-FRCM strengthening system, the relevant design methods for RC beams with the FRCM strengthening system or the FRP strengthening system were first assessed for their applicability to RC beams with C-FRCM strengthening system, including American Specifications (ACI 549.4R-20 [63], AC 434-0616-R1 [64], ACI 440.2R-17 [65]), European Code (FIB Bulletin 14) [66], and Chinese Code (CECS 146-2003 (2007)) [67]. In the assessment, the bending capacities of specimens were calculated using these design specifications and then compared with the bending capacities obtained from the available experimental results in the literature and FEA simulations in this study.

6.2. Assessment of current design rules

It is worth noting that ACI 549.4R-20 [63] and AC 434-0616-R1 [64] are referenced for FRCM strengthening, while ACI 440.2R-17 [65], FIB Bulletin 14 [66] and CECS 146-2003 (2007) [67] are specified for FRP strengthening. For the design prediction of the bending capacities of RC beams, the above design codes [63-67] are derived from the theory of elasticity, which are based on the following basic assumptions: (a) Plane sections remain plane after loading; (b) Bonding between FRCM (FRP) and concrete substrate remains effective; (c) There is no relative slip between external FRCM (FRP) strengthening and the concrete; (d) FRCM has a bilinear behaviour to failure where only the second linear part of the curve is used in analysis and design; and (e) The linear elastic stress-strain relationship is adopted for FRP.

Commented [FW(3]: Dangling modifier!!!! 悬垂结构问题就是逗号前的动作不是主语发出的。

The bending capacities predicted from ACI 549.4R-20 [63] and AC 434-0616-R1 [64] should be reduced by multiplying strength reduction factor (Φ_m) detailed in ACI 318 [54]. The bending capacity contributed by FRP predicted from ACI 440.2R-17 [65] should be reduced by multiplying an additional reduction factor (ψ_f) for FRP, taken as 0.85 herein. In the FIB Bulletin 14 [66], stress block centroid coefficient (δ_G) and stress block area coefficient (ψ) are defined according to the failure modes. Bending capacity formulas in CECS 146-2003 (2007) [67] are given in accordance with the relative compressive height. Detailed calculation theories and formulas for the examined design specifications are provided by Feng et al. [37], while a brief summary is presented in Table 8. It is worth noting that the calculation formulas of ACI 549.4R-20 [63] and AC 434-0616-R1 [64] are essentially identical.

The comparisons of the bending capacities between all FEA results and the design code calculation results are shown in Table 7. It can be found that the bending capacities obtained from

FEA (M_{uf}) are greater than those calculated by the design formulas from ACI 549.4R-20 [63] and AC 434-0616-R1 [64] (M_{u1}), ACI 440.2R-17 [65] (M_{u2}), FIB Bulletin 14 [66] (M_{u3}), and CECS 146-2003 (2007) [67] (M_{u4}). The mean values of the M_{uf}/M_{u1}, the M_{uf}/M_{u2}, the M_{uf}/M_{u3} and the M_{uf}/M_{u4} ratios are 1.32, 1.40, 1.22 and 1.44, respectively, and the corresponding COVs are 0.068, 0.061, 0.075, 0.078, respectively. The bending capacities calculated by ACI 549.4R-20 [63], AC 434-0616-R1 [64], ACI 440.2R-17 [65] are more conservative than those obtained from FIB Bulletin 14 [66] and CECS 146-2003 (2007) [67]. The conservatism in all the examined design codes may be attributed to the fact that the design codes [63-67] adopt the elastic modulus after FRCM cracking that is much smaller than the elastic modulus before FRCM cracking, which leads to conservative calculations. In addition, a reduction factor is introduced to further reduce the bending capacity of the beam, resulting in extremely conservative results.

6.3. Proposed design formula

A new design formula for RC beam with C-FRCM strengthening system was proposed in this study. The proposed design moment prediction (M_{up}) was obtained essentially by modifying current moment prediction (M_{u3}) in FIB Bulletin 14 [66] by a correction factor (Θ), as shown in Eq. 31,

$$M_{up}=\Theta M_{u3} \tag{31}$$

where the correction factor (Θ) is proposed to consider the layer of CF mesh and complete wrapping as well as degree of corrosion of steel bar, by calibration through comparisons with the test and numerical results, as given in Eq. 32,

$$\Theta = b_0 + b_1 L_{CF} + b_2 L_{CF}^2 + b_3 L_U + b_4 L_U^2 + b_5 \rho + b_6 \rho^2 \tag{32}$$

where L_{CF} and L_U are the layers of CF mesh and complete wrapping, respectively, and the values of both ranged from 1 to 3; ρ% is the degree of corrosion of steel bar, and ρ ranged from 0 to 10; while b_0, b_1, b_2, b_3, b_4, b_5 and b_6 are the coefficients determined by the multivariate regression analysis based on the FEA and test results in the parametric study.

It is worth noting that the design form of Eq. 32 was based on observations of the test and FEA results, rather than a random mathematical form. From the strengthening effect analysis in Section 5.3, it can be seen that the relationships between the layer of CF mesh, the layer of complete wrapping or the corrosion degree of steel bars and the strengthening effect are nonlinear, with at least two order function. From the perspective of constructing a relatively simple and feasible fitting

formula, each of the above parameters and correction factor (Θ) should be constructed with at least quadratic terms.

Finally, the bending capacity formula of the RC beam with C-FRCM strengthening system is given as follows:

$$\begin{aligned} M_{up} &= \Theta M_{u3} \\ &= \left(1.477 - 0.151L_{CF} - 0.010L_{CF}^2 + 0.052L_U - 0.013L_U^2 - 0.003\rho + 0.001\rho^2\right) \\ &\times \left[A_s f_y \left(d - \delta_G C\right) + A_f E_f \varepsilon_f \left(h - \delta_G C\right) + A_s' E_s \varepsilon_s' \left(\delta_G C - a'\right)\right] \end{aligned} \quad (34)$$

It is shown in Table 7 that the mean value of the M_u/M_{up} ratio is 1.00, with the COV of 0.037. Therefore, the proposed design formula can accurately predict the bending capacity of RC beam with the C-FRCM strengthening system.

7. Conclusions

This paper presents the effect of C-FRCM strengthening system on the bending behaviour of uncorroded and corroded RC beams. A parametric study comprising 35 supplementary RC beam models was conducted, highlighting the effects of the layer of CF mesh and complete wrapping and the degree of corrosion of steel bar on the bending capacity. The following conclusions can still be drawn:

- FEA can effectively predict the failure mode and strengthening performance of RC specimens with appropriate interface elements and interface constitutive theory. As for strengthened corroded RC members, the slip between CF mesh and cementitious matrix determines the stress response of RC members with C-FRCM system beyond the peak bending capacity and thus interface simulation is particularly critical.
- The ductility of RC beam retained well with one or two layers of CF mesh, yet the combination of the C-FRCM plate and the complete wrapping as the end anchorage is more effective than the C-FRCM plate only. The increase of the layer of CF mesh in the C-FRCM plate or complete wrapping will enhance the strengthening effect. Considering the optimum strengthening effect and maximum ductility retention using C-FRCM strengthening system, integration of the two-layer of C-FRCM plate and the three-layer complete wrapping is recommended.
- The current design codes, including ACI 549.4R-20 [63], AC 434-0616-R1 [64], ACI

440.2R-17 [65] and CECS 146-2003 (2007) [67], generally provide more conservative estimations on the bending capacities of corroded RC beams with C-FRCM strengthening system, compared with FIB Bulletin 14 [66]. It can result in inaccurate prediction of bending capacity for the examined strengthened beam.

- The modified calculation method in Bulletin 14 [66] can provide a more accurate estimation on RC beams fully considering the effects of the layer of CF mesh and complete wrapping, and the degree of corrosion of steel bar, which can be adopted for predicting flexural capacity of strengthened RC beam with C-FRCM strengthening system.

Acknowledgements

The authors are grateful for the financial support from Key-Area Research and Development Program of Guangdong Province (Grant No. 2019B111107002), National Key Research and Development Program of China (Grant No. 2018YFE0124900), National Natural Science Foundation of China (Grant Nos. 52178131/51538007/51778370/51861165204), Shenzhen Science and Technology Program (Grant No. GXWD20201230155427003-20200804174353001). The authors would like to thank Ms Beichen Liu for her assistance in the data processing of the research programme.

References

[1] Karbhari VM, Eckel DA. Effects of short-term environmental exposure on axial strengthening capacity of composite jacketed concrete. Journal of Composites, Technology and Research, 1995, 17(2): 99-106.

[2] Hou BR, Li XG, Ma XM, Du CW, Zhang DW, Zheng M, Xu WC, Lu DZ, Ma FB. The cost of corrosion in China. npj Materials Degradation, 2017, 1(1): 4.

[3] Vaysburd AM, Emmons PH. How to make today's repairs durable for tomorrow-corrosion protection in concrete repair. Construction and Building Materials, 2000, 14(4): 189-197.

[4] Li CQ, Yang Y, Melchers RE. Prediction of reinforcement corrosion in concrete and its effects on concrete cracking and strength reduction. ACI Materials Journal, 2008, 105(1): 3-10.

[5] Fan L, Teng L, Tang F, Khayat KH, Chen G, Meng W. Corrosion of steel rebar embedded in UHPC beams with cracked matrix. Construction and Building Materials, 2021, 313: 125589.

[6] Das JK, Pradhan B. Study on influence of nitrite and phosphate based inhibiting admixtures on chloride interaction, rebar corrosion, and microstructure of concrete subjected to different chloride exposures. Journal of Building Engineering, 2022, 50: 104192.

[7] Kim SJ, Smith ST. Pullout strength models for FRP anchors in uncracked concrete. Journal of Composites for Construction, ASCE 2010, 14(4): 406-414.

[8] Zhang HW, Smith ST, Gravina RJ, Wang ZY. Modelling of FRP-concrete bonded interfaces containing FRP anchors. Construction and Building Materials, 2017, 139: 394-402.

[9] Sun W, Liu HF, Wang YJ, He T. Impacts of configurations on the strength of FRP anchors. Composite Structures, 2018, 194: 126-135.

[10] Ozbakkaloglu T, Fang CF, Gholampour A. Influence of FRP anchor configuration on the behavior of FRP plates externally bonded on concrete members. Engineering Structures, 2017, 133: 133-150.

[11] Flores IAC, Gomez JF, Llaurado PV. Influence of multiple anchor arrangement in the behaviour of FRP-to-concrete anchored joints. Composite Structures, 2019, 230: 111528.

[12] Yang JQ, Smith ST, Wang ZY, Lim YY. Numerical simulation of FRP-strengthened RC slabs anchored with FRP anchors. Construction and Building Materials, 2018, 172: 735-750.

[13] Al-Sammari AT, Breña SF. Finite element simulation and parametric study of anchored

fiber-reinforced polymer sheets. ACI Materials Journal, 2018, 115(2): 365-377.
[14] Nayak AN, Kumari A, Swain RB. Strengthening of RC beams using externally bonded fibre reinforced polymer composites. Structures, 2018, 14: 137-152.
[15] Hawileh RA, Musto HA, Abdalla JA, Naser MZ. Finite element modeling of reinforced concrete beams externally strengthened in flexure with side-bonded FRP laminates. Composites Part B: Engineering, 2019, 173: 106952.
[16] Phan VT, Nguyen DD. Efficiency of flexural strengthening RC beams using fiber reinforced polymer materials. Materials Today: Proceedings, 2021, 38: 2584-2589.
[17] Sengun K, Arslan G. Parameters affecting the behaviour of RC beams strengthened in shear and flexure with various FRP systems. Structures, 2022, 40: 202-212.
[18] Hawileh RA, Mhanna HH, Rashed AA, Abdalla JA, Naser MZ. Flexural behavior of RC beams externally bonded with polyethylene terephthalate (PET) fiber reinforced polymer (FRP) laminates. Engineering Structures, 2022, 256: 114036.
[19] Liu XF, Li Y. Static bearing capacity of partially corrosion-damaged reinforced concrete structures strengthened with PET FRP composites. Construction and Building Materials, 2019, 211: 33-43.
[20] Ling ZB, Liu WQ, Shao JS. Experimental and theoretical investigation on shear behaviour of small-scale timber beams strengthened with Fiber-Reinforced Polymer composites. Composite Structures, 2020, 240: 111989.
[21] Sai Krishna M, Sandeep Kumar GAVS, Cyril Thomas A. Behaviour of reinforced concrete beams bonded with side bonded FRP sheets. Materials Today: Proceedings, 2021, 43: 2404-2410.
[22] Ke Y, Zhang SS, Nie XF, Yu T, Yang YM, Jedrzejko MJ. Finite element modelling of RC beams strengthened in flexure with NSM FRP and anchored with FRP U-jackets. Composite Structures, 2022, 282: 115104.
[23] Fathalla E, Rajapakse RMCM, Mihaylov BI. Modeling the shear behavior of deep beams strengthened with FRP sheets. Engineering Structures, 2022, 260: 114232.
[24] Ebead U, El-Sherif H. Near surface embedded-FRCM for flexural strengthening of reinforced concrete beams. Construction and Building Materials, 2019, 204: 166-176.
[25] El-Sherif H, Wakjira TG, Ebead U. Flexural strengthening of reinforced concrete beams using hybrid near-surface embedded/externally bonded fabric-reinforced cementitious matrix.

Construction and Building Materials, 2020, 238: 117748.
[26] Hadad HA, Erickson B, Nanni A. Flexural analysis and design of FRCM-strengthened RC beams. Construction and Building Materials, 2020, 244: 118371.
[27] Mandor A, El Refai A. Strengthening the hogging and sagging regions in continuous beams with fiber-reinforced cementitious matrix (FRCM): Experimental and analytical investigations. Construction and Building Materials, 2022, 321: 317-329.
[28] Mandor A, El Refai A. Flexural response of reinforced concrete continuous beams strengthened with fiber-reinforced cementitious matrix (FRCM). Engineering Structures, 2022, 251: 113557.
[29] Wakjira TG, Ibrahim M, Ebead U, Alam MS. Explainable machine learning model and reliability analysis for flexural capacity prediction of RC beams strengthened in flexure with FRCM. Engineering Structures, 2022, 255: 113903.
[30] Su MN, Wei LL, Zhu JH. Combined impressed current cathodic protection and FRCM strengthening for corrosion-prone concrete structures. Journal of Composites for Construction, ASCE 2019, 23(4): 04019021.
[31] Zhu JH, Su MN, Huang JY, Ueda T, Xing F. The ICCP-SS technique for retrofitting reinforced concrete compressive members subjected to corrosion. Construction and Building Materials, 2018, 67(10): 669-679.
[32] Khattak N, Mansour M, El-Maaddawy T, Ismail N. Continuous reinforced concrete beams strengthened with fabric-reinforced cementitious matrix: Experimental Investigation and Numerical Simulation. Buildings, 2022, 12(1): 27.
[33] Abdulla K, Zhu XM, Su MN. Numerical investigation of FRCM-strengthened corroded RC beams under cathodic protection. Materials (Basel, Switzerland), 2022, 15(15): 5334.
[34] Mercedes L, Escrig C, Bernat-Masó E, Gil L. Analytical approach and numerical simulation of reinforced concrete beams strengthened with different FRCM systems. Materials, 2021, 14(8): 1857.
[35] Aljazaeri ZR, Al-Jaberi Z. Numerical study on flexural behavior of concrete beams strengthened with fiber reinforced cementitious matrix considering different concrete compressive strength and steel reinforcement ratio. International Journal of Engineering, 2021, 34(4): 793-802.
[36] Bertolesi E, Milani G, Poggi C. Simple holonomic homogenization model for the non-linear

static analysis of in-plane loaded masonry walls strengthened with FRCM composites. Composite Structure, 2016, 158: 291-307.

[37] Feng R, Liu YX, Zhu JH, Xing F. Flexural behaviour of C-FRCM strengthened corroded RC continuous beams. Composite Structures, 2020, 245: 112200.

[38] Manie J, Kikstra WP. DIANA Finite Element Analysis, Release 9.4.4 User's manual. TNO DIANA BV, Delft, The Netherlands, 2014.

[39] Vecchio FJ, Collins MP. The modified compression field theory for reinforced concrete elements subjected to shear. ACI Journal, 1986, 83(2): 219-231.

[40] Selby RG, Vecchio FJ. Three-dimensional Constitutive Relations for Reinforced Concrete. Technical Report 93-02. Department Civil Engineering, University of Toronto, Toronto, Canada, 1993.

[41] You YM, Ayoub A, Belarbi A. Three-dimensional nonlinear finite-element analysis of prestressed concrete beams strengthened in shear with FRP composites. Journal of Composites for Construction, ASCE 2011, 15(6): 896-907.

[42] Kataoka MN, Ferreira MA, Homce de Cresce El Debs, Ana Lucia. Nonlinear FE analysis of slab-beam-column connection in precast concrete structures. Engineering Structures, 2017, 143(15): 306-315.

[43] Araujo DDL, Prado LP, Da Silva EB, El Debs MK. Temporary beam-to-column connection for precast concrete frame assembly. Engineering Structures, 2018, 171: 529-544.

[44] Hordijk DA. Local Approach to Fatigue of Concrete. PhD thesis, Delft University of Technology, Delft, The Netherlands, 1991.

[45] Bazant ZP, Oh BH. Crack band theory for fracture of concrete. Materials and Structures, 1983, 16(93): 155-177.

[46] Feenstra PH. Computational Aspects of Biaxial Stress in Plain and Reinforced Concrete. PhD thesis, Delft University of Technology, Delft, The Netherlands, 1993.

[47] GB 50010-2010. Code for Design of Concrete Structures. Ministry of Housing and Urban-Rural Development of the People's Republic of China, Beijing, China, 2015. (in Chinese)

[48] Wu Q, Yuan YS. Experimental study on the deterioration of mechanical properties of corroded reinforcing bars. China Civil Engineering Journal, 2008, 12(41): 42-47. (in Chinese)

[49] Akbas T, Celik OC, Yalcin C, Ilki A. Monotonic and cyclic bond behavior of deformed CFRP

bars in high strength concrete. Polymers, 2016, 8(6): 211.
[50] CEB-FIP Model Code. Design of Concrete Structures. British Standard Institution, London, UK, 1993.
[51] Xu SH. The Models of Degradation and Durability Evaluation of Reinforced Concrete Structure. PhD thesis, College of Civil Engineering, Xi'an University of Architecture and Technology, Xi'an, China, 2003. (in Chinese)
[52] Obaidat YT, Heyden S, Dahlblom O. The effect of CFRP and CFRP/concrete interface models when modelling retrofitted RC beams with FEM. Composite Structures, 2010, 92(6): 1391-1398.
[53] Sakr MA. Finite element modelling of debonding mechanisms in carbon fiber reinforced polymer-strengthened reinforced concrete continuous beams. Structural Concrete: Journal of the FIB, 2018, 19(4): 1002-1012.
[54] ACI 318-08. Building Code Requirement for Structural Concrete and Commentary. Farmington Hills, MI 48331, USA, 2008.
[55] Zhu MC. Bond Behaviour and Degradation Mechanisms of Multi-Functional Fabric Reinforced Cementitious Matrix (MFRCM) Composites used for ICCP-SS. PhD thesis, Hokkaido University, Sapporo, Hokkaido, Japan, 2020.
[56] Tian J, Wu XW, Zheng Y, Hu SW, Du YF, Wang WW, Sun C, Zhang LF. Investigation of interface shear properties and mechanical model between ECC and concrete. Construction and Building Materials, 2019, 223: 12-27.
[57] Lu XZ, Ye LP, Teng JG, Zhuang JB. Bond-slip model for FRP-to-concrete interface. Journal of Building Structures, 2005, 04: 10-18. (in Chinese)
[58] Wei LL, Ueda T, Matsumoto K, Zhu JH. Experimental and analytical study on the behavior of RC beams with externally bonded carbon-FRCM composites. Composite structures, 2021, 273: 114291.
[59] Bencardino F, Carloni C, Condello A, Focacci F, Napoli A, Realfonzo R. Flexural behaviour of RC members strengthened with FRCM: State-of-the-art and predictive formulas. Composites, 2018, 148B: 132-148.
[60] Pellegrino C, D'Antino T. Experimental behaviour of existing precast prestressed reinforced concrete elements strengthened with cementitious composites. Composites Part B: Engineering, 2013, 55: 31-40.

[61] Sneed LH, Verre S, Carloni C, Ombres L. Flexural behavior of RC beams strengthened with steel-FRCM composite. Engineering Structures, 2016, 127: 686-699.

[62] Escrig C, Gil L, Bernat-Maso E. Experimental comparison of reinforced concrete beams strengthened against bending with different types of cementitious-matrix composite materials. Construction and Building Materials, 2017, 137: 317-329.

[63] ACI 549.4R-20. Guide to Design and Construction of Externally Bonded Fabric-Reinforced Cementitious Matrix (FRCM) Systems for Repair and Strengthening Concrete and Masonry Structures. American Concrete Institute, Farmington Hills, USA, 2020.

[64] AC 434-0616-R1. Proposed Revisions to the Acceptance Criteria for Masonry and Concrete Strengthening using Fabric-Reinforced Cementitious Matrix (FRCM) Composite Systems. ICC Evaluation Service, Washington, DC, USA, 2016.

[65] ACI 440.2R-17. Guide for the Design and Construction of Externally Bonded FRP Systems for Strengthening Concrete Structures. American Concrete Institute, Farmington Hills, USA, 2017.

[66] FIB Bulletin 14. Externally Bonded FRP Reinforcement for RC Structures. International Federation for Structural Concrete, Zürich, Switzerland, 2001.

[67] CECS 146-2003 (2007). Technical Specification for Strengthening Concrete Structures with Carbon Fiber Reinforced Polymer Laminate. China Association for Engineering Construction Standardization, Beijing, China, 2007. (in Chinese)

Notations

a_1	Ratio of prismatic compressive strength to cubic compressive strength
a_2	Brittleness reduction coefficient of high-strength concrete
a'	Distance from top of beam to centroid of longitudinal compressive bar
A_{cf}	Cross-sectional area of carbon yarn
A_s	Area of longitudinal tensile bar
A_s'	Area of longitudinal compressive bar
c_{cf}	Perimeter of a single carbon yarn
C	Compression force provided by concrete
E_{cf}	Elastic modulus of CF mesh
E_{cm}	Elastic modulus of cementitious matrix
E_{lu}	Elastic modulus of longitudinal bar
E_{su}	Elastic modulus of stirrup
E_u	Elastic modulus of complete wrapping
E_{uc}	Elastic modulus of corroded steel bar
E_{u0}	Elastic modulus of uncorroded steel bar
f_c	Axial compressive strength of concrete
f_c'	Compressive strength of concrete cylinder
f_{cmc}	Compressive strength of cementitious matrix
f_{cmt}	Tensile strength of cementitious matrix
f_{cu}	Compressive strength of concrete cube
f_{lu}	Ultimate strength of longitudinal bar
f_{ly}	Yield strength of longitudinal bar
f_{su}	Ultimate strength of stirrup
f_{sy}	Yield strength of stirrup
f_t	Axial tensile strength of concrete
$f_t^{'ef}$	Effective tensile strength of concrete
f_{uc}	Ultimate strength of corroded steel bar
f_{u0}	Ultimate strength of uncorroded steel bar
f_{yc}	Yield strength of corroded steel bar

1	f_{y0}	Yield strength of uncorroded steel bar
2	G_a	Elastic shear modulus of epoxy resin layer involved in shear
3	G_c	Compressive fracture energy of concrete
4	G_{ck}	Elastic shear modulus of concrete
5	G_f	Fracture energy in creating a fracture surface of unit area of concrete
6	G_{uf}	Total interface failure energy
7	h	Height of beam
8	h_l	Characteristic element length
9	h_0	Effective height of beam section
10	k_1	Slope of elastic segment
11	k_2	Slope of debonding segment
12	K_a	Shear stiffness of epoxy resin layer
13	K_c	Shear stiffness of concrete substrate involved in shear deformation
14	K_0	Initial stiffness of bond-slip relationship of complete wrapping and concrete
15	L	Bonding length of carbon yarn
16	$L_t^{'}$	Length of failure zone of concrete in tension
17	M_{ef1}	Elastic moment at mid-support obtained from FEA
18	M_{ef2}	Elastic moment at mid-span obtained from FEA
19	M_f	Moment contribution of FRCM reinforcement to bending capacity
20	M_s	Moment contribution of longitudinal bar to bending capacity
21	M_{uf}	Ultimate bending capacity determined by FEA
22	M_{uf1}	Ultimate moment at mid-support determined by FEA
23	M_{uf2}	Ultimate moment at mid-span determined by FEA
24	M_{up}	Ultimate bending capacity calculated by proposed formula
25	M_{ut}	Ultimate bending capacity obtained from test
26	M_{u1}	Ultimate bending capacity calculated by ACI 549.4R-20 and AC 434-0616-R1
27	M_{u2}	Ultimate bending capacity calculated by ACI 440.2R-17
28	M_{u3}	Ultimate bending capacity calculated by FIB Bulletin 14
29	M_{u4}	Ultimate bending capacity calculated by CECS 146-2003 (2007)
30	P	Applied load in pullout test
31	P_{uf}	Ultimate load obtained from FEA

P_{ut}	Ultimate load obtained from test
s	Local slip between steel and concrete
s_{cm}	Interface slip of ECC-to-concrete interface
s_{cmu}	Ultimate interface slip of ECC-to-concrete interface
s_{cm0}	Interface slip corresponding to ultimate shear strength
s_{ue}	Elastic part of slippage at interface between complete wrapping and beam
t_a	Thickness of epoxy resin layer involved in shear
t_c	Effective thickness of concrete substrate participating in shear deformation under interface
u	Pullout displacement
u_u	Displacement corresponding to the ultimate load
u_y	Corresponding displacement when the longitudinal bar yields
α_c	Concrete strain at which the maximum compressive strength is reached
$\alpha_{c/3}$	Concrete strain at which one-third of the maximum compressive strength is reached
α_u	Concrete ultimate strain at which material is completely softened in compression
β	Correction coefficient of bonding strength between steel bar and concrete
β_w	Width influence coefficient of FRP-concrete
β_{1f}	Moment redistribution at mid-support determined by FEA
β_{1t}	Moment redistribution at mid-support obtained from test
β_{2f}	Moment redistribution at mid-span determined by FEA
β_{2t}	Moment redistribution at mid-span obtained from test
ε_{eq}	Effective uniaxial tensile strain of concrete
ε_{lu}	Ultimate strain of longitudinal bar
ε_s	Ultimate strain of corroded steel bar
ε_{sc}	Ultimate strain of uncorroded steel bar
ε_{su}	Ultimate strain of stirrup
ε_{tu}	Ultimate tensile strain of CF mesh
$[\varepsilon_{cf}]$	Allowable tensile strain of FRP
τ	Local bonding strength between concrete and steel bar
τ_{cm}	Shear stress of ECC-to-concrete interface
τ_{cmu}	Ultimate shear strength of ECC-to-concrete interface

τ_{max}	The maximum local bonding strength between concrete and steel bar
$\tau_{max,cf}$	The maximum bonding stress between carbon yarn and cementitious matrix
$\tau_{0,cf}$	Bonding stress during friction segment
λ_1	Temporary variable of elastic segment
λ_2	Temporary variable of debonding segment
$\rho\%$	Degree of corrosion of steel bar
w	Crack opening displacement
w_c	Crack opening displacement when stress is fully released
υ_{cf}	Poisson's ratio of CF mesh
υ_u	Poisson's ratio of complete wrapping
δ_G	Stress block centroid coefficient
δ_u	Ductility index
σ	Normal stress of concrete in crack direction
σ_{cm}	Uniaxial compressive strength of ECC
χ	Interface roughness value of ECC-to-concrete interface
ξ_b	Relative compressive height coefficient of longitudinal rebar
ξ_{cfb}	Limit relative compression height when FRP reaches its allowable tensile strain and concrete is crushed at the same time
Φ_m	Strength reduction factor
Ψ	Stress block area coefficient
ψ_f	Reduction coefficient of additional capacity of FRP
Θ	Correction coefficient of bending capacity formula

Group	Specimen	Layer of CF mesh	Layer of complete wrapping	Degree of corrosion of steel bar (%)
Uncorroded beam	B-L0-U0	0	0	0.00
	B-L2-U0	2	0	0.00
	B-L3-U0	3	0	0.00
	B-L2-U3	2	3	0.00
	B-L3-U2	3	2	0.00
Corroded beam	CB-L0-U0	0	0	5.96
	CB-L2-U0	2	0	4.00
	CB-L3-U0	3	0	5.79
	CB-L2-U3	2	3	6.93
	CB-L3-U2	3	2	2.22

Table 1. Group setting of RC continuous beams

Material	Material property	Uncorroded specimen	CB-L0-U0	CB-L2-U0	CB-L3-U0	CB-L2-U3	CB-L3-U2
Longitudinal rebar	f_{ly} (MPa)	480.00	380.91	424.32	386.13	351.11	449.10
	f_{lu} (MPa)	602.00	487.91	539.39	494.25	451.70	567.25
	ε_{lu} (%)	7.14	4.70	5.50	4.80	4.29	6.23
	E_{lu} (GPa)	200.00	142.03	158.40	143.10	136.03	176.91
Stirrup	f_{sy} (MPa)	412.00	326.95	364.21	331.43	301.37	385.98
	f_{su} (MPa)	572.00	463.59	512.51	469.62	429.19	538.98
	ε_{su} (%)	12.00	7.90	9.20	8.00	7.22	10.47
	E_{su} (GPa)	200.00	142.03	158.40	143.10	136.03	176.91
Concrete	f_t (MPa)	2.01					
	f_c (MPa)	34.50					
	f_{cu} (MPa)	52.00					
	E_c (GPa)	30.00					
Cementitious matrix	f_{cmt} (MPa)	5.50					
	f_{cmc} (MPa)	78.80					
	E_{cm} (GPa)	30.00					
CF mesh	E_{cf} (GPa)	132.00					
	υ_{cf}	0.20					
Complete wrapping	E_u (GPa)	240.00					
	υ_u	0.20					

Table 2. Summary of material properties in FEA

Parameter	Ribbed steel bar
s_1 (mm)	0.60
s_2 (mm)	0.60
s_3 (mm)	1.00
α	0.40
τ_{max} (MPa)	$2.0\sqrt{f_c'}$
τ_f (MPa)	$0.15\tau_{max}$

Table 3. Parameters of steel bar bond-slip constitutive theory

Roughness	f_{cmc}	s_{cm0}	s_{cmu}	a	b	c	τ_{cmu}
0.57	78.8	0.765	0.981	-0.04334	-1.69877	0.04589	1.17
0.57	78.8	0.765	0.981	-0.08155	-0.84199	0.06987	2.24
0.57	78.8	0.765	0.981	-0.09284	-0.80271	0.06067	1.18
0.57	78.8	0.765	0.981	-0.07562	-1.21648	0.07555	2.22
0.57	78.8	0.765	0.981	-0.10478	-0.95987	0.08487	2.13
1.33	78.8	1.055	1.105	-0.04334	-1.69877	0.04589	2.06
1.33	78.8	1.055	1.105	-0.08155	-0.84199	0.06987	4.18
1.33	78.8	1.055	1.105	-0.09284	-0.80271	0.06067	3.39
1.33	78.8	1.055	1.105	-0.07562	-1.21648	0.07555	3.96
1.33	78.8	1.055	1.105	-0.10478	-0.95987	0.08487	4.62
3.33	78.8	1.206	1.164	-0.04334	-1.69877	0.04589	3.14
3.33	78.8	1.206	1.164	-0.08155	-0.84199	0.06987	5.38
3.33	78.8	1.206	1.164	-0.09284	-0.80271	0.06067	4.67
3.33	78.8	1.206	1.164	-0.07562	-1.21648	0.07555	5.57
3.33	78.8	1.206	1.164	-0.10478	-0.95987	0.08487	6.43

Table 4. Parameters of bonding strength between cementitious matrix and concrete

Mesh size (mm)	20	30	40
Calculation time	48 hours	4 hours	2 hours
Ultimate capacity obtain from test (kN)	275.19	275.19	275.19
Ultimate capacity obtain from FEA (kN)	265.18	273.73	299.21
Difference (%)	-3.64	-0.53	8.73

Table 5. Mesh sensitivity analysis

Specimen	P_{ut}	P_{uf}	P_{ut}/P_{uf}	M_{ut}	M_{uf}	M_{ut}/M_{uf}
B-L0-U0	250.03	252.52	0.99	23.47	24.09	0.97
B-L2-U0	268.26	265.06	1.01	26.00	22.74	1.14
B-L3-U0	265.31	279.63	0.95	25.87	24.49	1.06
B-L2-U3	275.19	273.37	1.01	27.72	24.26	1.14
B-L3-U2	285.14	285.00	1.04	28.24	25.63	1.10
CB-L0-U0	218.82	216.61	1.01	20.33	20.58	0.99
CB-L2-U0	225.35	242.58	0.93	23.01	22.01	1.05
CB-L3-U0	224.05	241.61	0.93	22.23	21.63	1.03
CB-L2-U3	238.18	235.10	1.01	24.12	21.17	1.14
CB-L3-U2	282.93	278.29	1.02	28.20	25.88	1.09
Mean			0.99	—		1.07
COV			0.037	—		0.059

Table 6. Comparison of ultimate loads obtained from tests and FE

Specimen	P_u (kN)	Degree of corrosion (%)	M_u (kN·m)	ACI 549.4R-20 [63] AC434-0616-R1 [64]		ACI 440.2R-17 [65]		FIB Bulletin 14 [66]		CECS 146-2003 (2007) [67]		M_{up}	M_u/M_{up}
				M_{u1} (kN·m)	M_u/M_{u1}	M_{u2} (kN·m)	M_u/M_{u2}	M_{u3} (kN·m)	M_u/M_{u3}	M_{u4} (kN·m)	M_u/M_{u4}	(kN·m)	
B-L0-U0	250.03	0.00	24.09	—	—	—	—	—	—	—	—	—	—
B-L1-U0	255.38	0.00	21.91	15.62	1.40	15.25	1.44	16.59	1.32	15.39	1.42	22.16	0.99
B-L2-U0	268.62	0.00	22.74	17.52	1.30	16.75	1.36	18.83	1.21	16.92	1.34	22.85	1.00
B-L3-U0	265.31	0.00	24.49	19.34	1.27	18.20	1.35	20.99	1.17	18.44	1.33	23.31	1.05
B-L1-U1	267.63	0.00	22.96	15.62	1.47	15.25	1.51	16.59	1.38	15.39	1.49	22.79	1.01
B-L1-U2	254.73	0.00	21.86	17.52	1.25	16.75	1.30	18.83	1.16	16.92	1.29	23.79	0.92
B-L1-U3	257.40	0.00	22.08	19.34	1.14	18.20	1.21	20.99	1.05	18.44	1.20	24.05	0.92
B-L2-U1	265.62	0.00	22.79	17.52	1.30	16.75	1.36	18.83	1.21	16.92	1.35	23.57	0.97
B-L2-U2	271.68	0.00	23.31	17.52	1.33	16.75	1.39	18.83	1.24	16.92	1.38	23.79	0.98
B-L2-U3	275.19	0.00	24.26	17.52	1.38	16.75	1.45	18.83	1.29	16.92	1.43	23.51	1.03
B-L3-U1	287.95	0.00	24.71	19.34	1.28	18.20	1.36	20.99	1.18	18.44	1.34	24.11	1.02
B-L3-U2	285.14	0.00	25.63	19.34	1.32	18.20	1.41	20.99	1.22	18.44	1.39	24.36	1.05
B-L3-U3	281.16	0.00	24.12	19.34	1.25	18.20	1.33	20.99	1.15	18.44	1.31	24.05	1.00
CB-L0-U0	218.82	5.96	20.58	—	—	—	—	—	—	—	—	—	—
CB-L1-U0	246.16	4.00	21.12	14.35	1.47	13.92	1.52	15.37	1.37	13.79	1.53	20.50	1.03
CB-L2-U0-i_1	225.35	2.00	22.45	16.97	1.32	16.16	1.39	18.32	1.23	16.11	1.39	22.15	1.01
CB-L2-U0	242.58	4.00	22.01	16.46	1.34	15.59	1.41	17.85	1.23	15.31	1.44	21.62	1.02
CB-L2-U0-i_3	234.07	6.00	20.08	15.45	1.30	14.54	1.38	16.81	1.19	14.02	1.43	20.49	0.98
CB-L2-U0-i_4	221.58	8.00	19.01	13.93	1.36	12.98	1.47	15.19	1.25	12.24	1.55	18.71	1.02
CB-L2-U0-i_5	206.58	10.00	17.72	12.43	1.43	11.43	1.55	13.58	1.30	10.46	1.69	16.99	1.04
CB-L3-U0-i_1	264.73	2.00	22.71	18.89	1.20	17.68	1.28	20.57	1.10	17.63	1.29	22.76	1.00
CB-L3-U0-i_2	252.80	4.00	21.69	18.47	1.17	17.19	1.26	20.22	1.07	16.83	1.29	22.40	0.97
CB-L3-U0	224.05	5.79	21.63	17.71	1.22	16.37	1.32	19.45	1.11	15.72	1.38	21.68	1.00
CB-L3-U0-i_3	237.32	6.00	20.36	17.56	1.16	16.21	1.26	19.28	1.06	15.54	1.31	21.52	0.95

CB-L3-U0-i_4	231.32	8.00	19.85	16.12	1.23	14.71	1.35	17.75	1.12	13.76	1.44	20.04	0.99
CB-L3-U0-i_5	206.08	10.00	17.68	14.71	1.20	13.24	1.34	16.24	1.09	11.99	1.48	18.65	0.95
CB-L1-U1	254.48	2.00	21.83	14.98	1.46	14.58	1.50	15.97	1.37	14.59	1.50	21.87	1.00
CB-L1-U2	253.32	2.00	21.74	14.98	1.45	14.58	1.49	15.97	1.36	14.59	1.49	22.06	0.99
CB-L1-U3	251.93	2.00	21.62	14.98	1.44	14.58	1.48	15.97	1.35	14.59	1.48	21.82	0.99
CB-L2-U1	237.36	6.93	20.37	14.74	1.38	13.81	1.48	16.05	1.27	13.19	1.54	20.27	1.01
CB-L2-U2	231.68	6.93	19.88	14.74	1.35	13.81	1.44	16.05	1.24	13.19	1.51	20.46	0.97
CB-L2-U3-i_1	260.37	2.00	22.34	16.97	1.32	16.16	1.38	18.32	1.22	16.11	1.39	22.80	0.98
CB-L2-U3-i_2	255.54	4.00	21.93	16.46	1.33	15.59	1.41	17.85	1.23	15.31	1.43	22.25	0.99
CB-L2-U3-i_3	240.44	6.00	20.63	15.45	1.34	14.54	1.42	16.81	1.23	14.02	1.47	21.08	0.98
CB-L2-U3	238.18	6.93	21.17	14.74	1.44	13.81	1.53	16.05	1.32	13.19	1.60	20.22	1.05
CB-L2-U3-i_4	229.04	8.00	19.65	13.93	1.41	12.98	1.51	15.19	1.29	12.24	1.61	19.24	1.02
CB-L2-U3-i_5	213.15	10.00	18.29	12.43	1.47	11.43	1.60	13.58	1.35	10.46	1.75	17.47	1.05
CB-L3-U1	278.56	2.22	23.90	18.84	1.27	17.62	1.36	20.53	1.16	17.54	1.36	23.50	1.02
CB-L3-U2-i_1	279.90	2.00	26.00	18.89	1.38	17.68	1.47	20.57	1.26	17.63	1.47	23.79	1.09
CB-L3-U2	282.93	2.22	25.88	18.84	1.37	17.62	1.47	20.53	1.26	17.54	1.48	23.74	1.09
CB-L3-U2-i_2	266.78	4.00	22.89	18.47	1.24	17.19	1.33	20.22	1.13	16.83	1.36	23.42	0.98
CB-L3-U2-i_3	257.07	6.00	22.06	17.56	1.26	16.21	1.36	19.28	1.14	15.54	1.42	22.48	0.98
CB-L3-U2-i_4	236.96	8.00	20.33	16.12	1.26	14.71	1.38	17.75	1.15	13.76	1.48	20.92	0.97
CB-L3-U2-i_5	221.70	10.00	19.02	14.71	1.29	13.24	1.44	16.24	1.17	11.99	1.59	19.46	0.98
CB-L3-U3	271.40	2.22	23.29	18.84	1.24	17.62	1.32	20.53	1.13	17.54	1.33	23.44	0.99
Mean					1.32		1.40		1.22		1.44		1.00
COV					0.068		0.061		0.075		0.078		0.037

Table 7. Comparison of bending capacities obtained from tests, FEA and design codes

Design code	Design formulas
ACI 549.4R-20 [63] AC 434-0616-R1 [64]	$M_{u1}=\Phi_m\left[A_s f_s\left(d-\frac{\beta_1 c}{2}\right)+A_s' f_s'\left(\frac{\beta_1 c}{2}-a'\right)+A_f f_{fe}\left(d_f-\frac{\beta_1 c}{2}\right)\right]$
ACI 440.2R-17 [65]	$M_{u2}=A_s f_s\left(d-\frac{\beta_1 c}{2}\right)+\psi_f A_f\left(d_f-\frac{\beta_1 c}{2}\right)$
FIB Bulletin 14 [66]	$M_{u3}=A_{s1} f_{yd}\left(d-\delta_G x\right)+A_f E_f \varepsilon_f\left(h-\delta_G x\right)+A_{s2} E_s \varepsilon_{s2}\left(\delta_G x-d_2\right)$
CECS 146-2003 (2007) [67]	$\xi_{cfb}h<x<\xi_b h_0$: $M_{u4}\le f_c b_f' x\left(h_0-\frac{x}{2}\right)+f_y' A_s'\left(h_0-a'\right)+\sigma_{f,md} A_f\left(h_{fe}-h_0\right)$ $x\le\xi_{cfb}h$: $M_{u4}\le f_c b x\left(h_0-\frac{x}{2}\right)+f_y' A_s'\left(h_0-a'\right)+E_{cf}\varepsilon_{cf} A_{cf}\left(h-h_0\right)$ $x<2a$: $M_{u4}\le f_y A_s\left(h_0-a'\right)+E_{cf}\left[\varepsilon_{cf}\right]A_{cf}\left(h-a'\right)$
Proposed formula	$M_{up}=\left(1.477-0.151L_{CF}-0.010L_{CF}^2+0.052L_U-0.013L_U^2-0.003\rho+0.001\rho^2\right)$ $\times\left[A_s f_y\left(d-\delta_G C\right)+A_f E_f \varepsilon_f\left(h-\delta_G C\right)+A_s' E_s \varepsilon_s'\left(\delta_G C-a'\right)\right]$

Table 8. Summary of design formulas for bending capacity

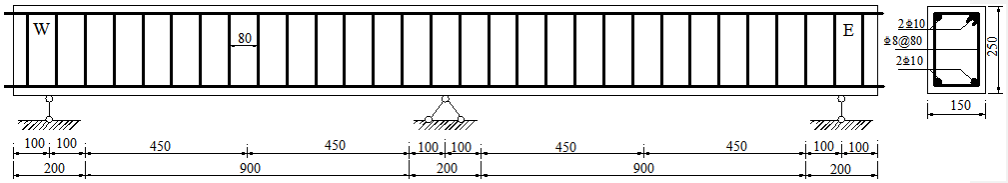

Figure 1. Details of beam specimens (unit: mm)

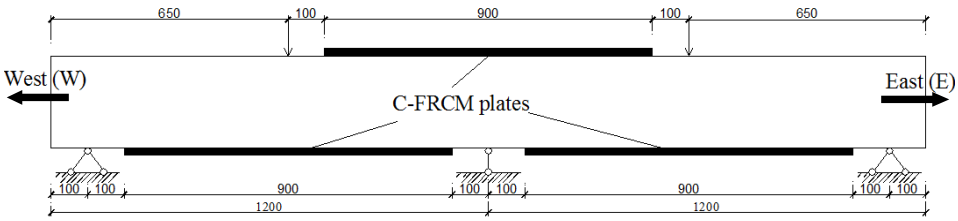

(a) Positions of C-FRCM plates

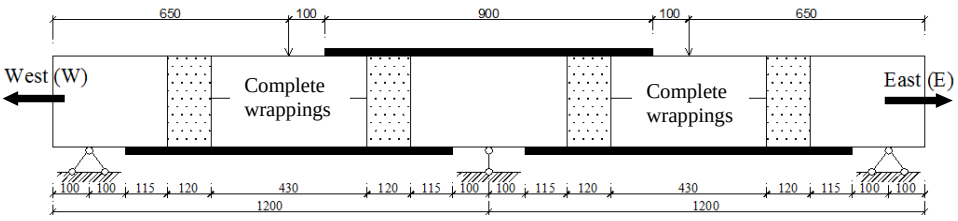

(b) Positions of complete wrappings

Figure 2. Positions of C-FRCM plates and complete wrappings (unit: mm)

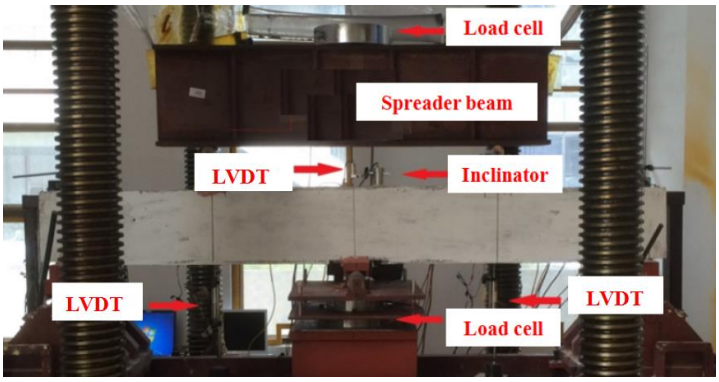

Figure 3. Test setup of RC continuous beam

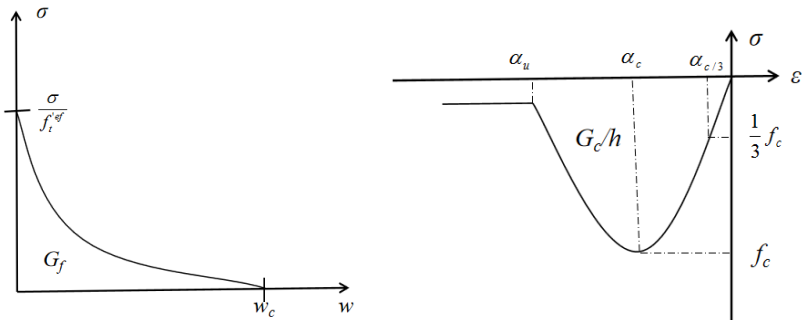

(a) Crack opening rule in Hordijk (b) Parabolic compression curve

Figure 4. Behaviour of concrete in tension and compression

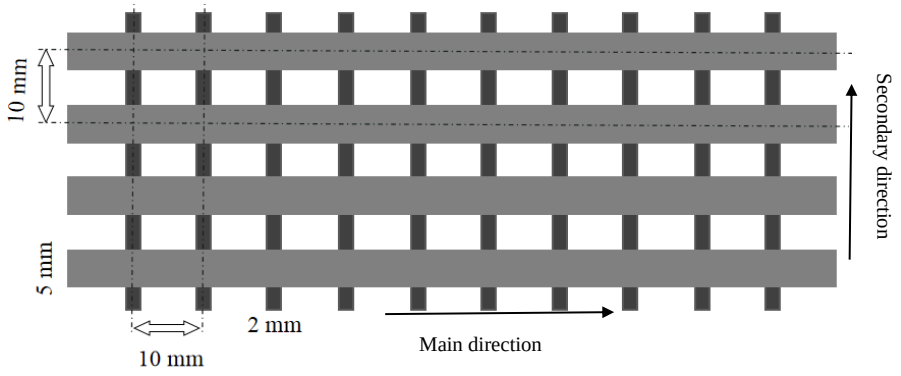

Figure 5. Mesh size and specification of CF mesh in C-FRCM plate

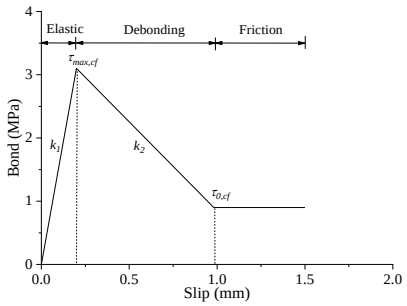

(a) Interface constitutive relationship between CF mesh and cementitious matrix

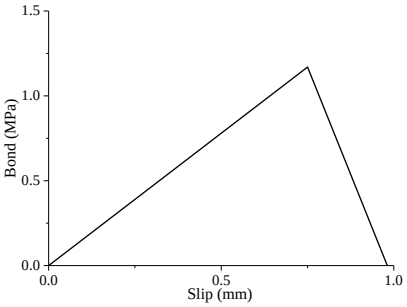

(b) Interface constitutive relationship between C-FRCM plate and concrete

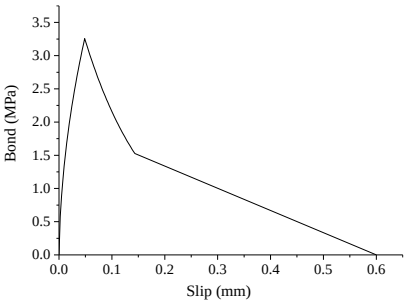

(c) Interface constitutive relationship between complete wrapping and concrete

Figure 6. Interface constitutive relationship

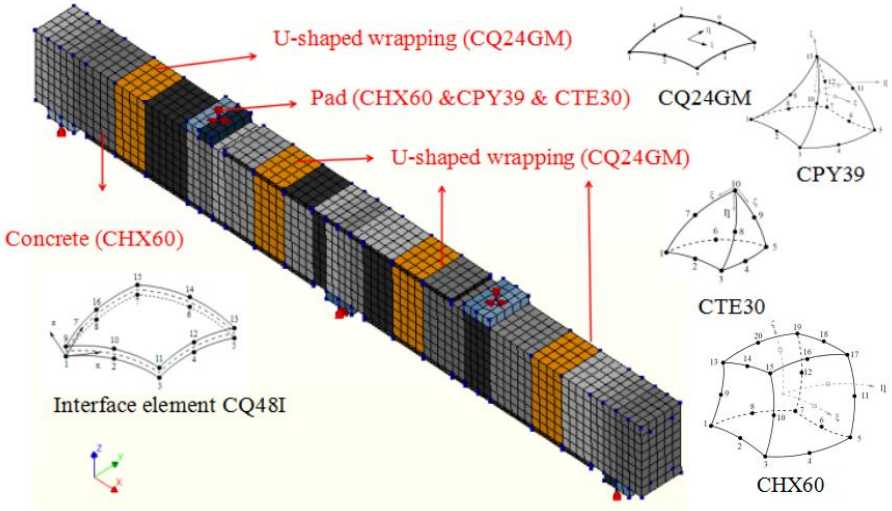

Figure 7. Finite element models of RC continuous beams

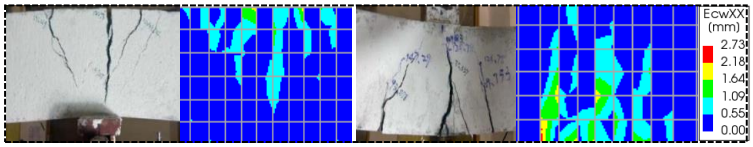

(a) Crack of concrete

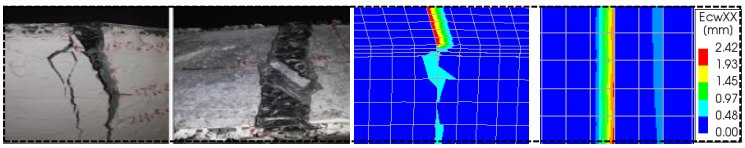

(b) Fracture of C-FRCM plate

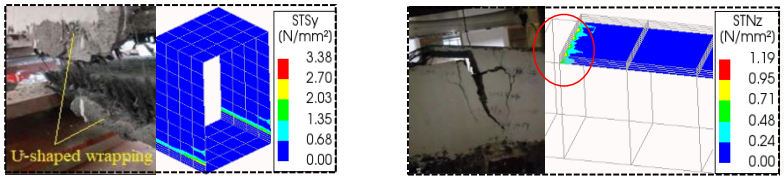

(c) Interface failure of complete wrapping (d) Interface failure between C-FRCM plate and concrete

Figure 8. Comparison of failure modes between tests and FEA

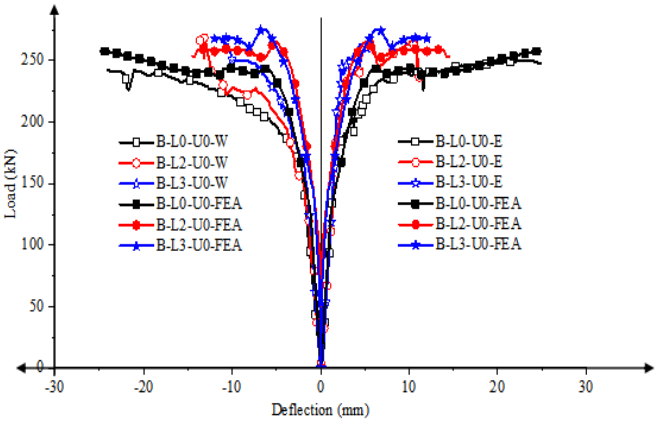

(a) Comparison of load-deflection curves of the specimens B-L0-U0, B-L2-U0 and B-L3-U0

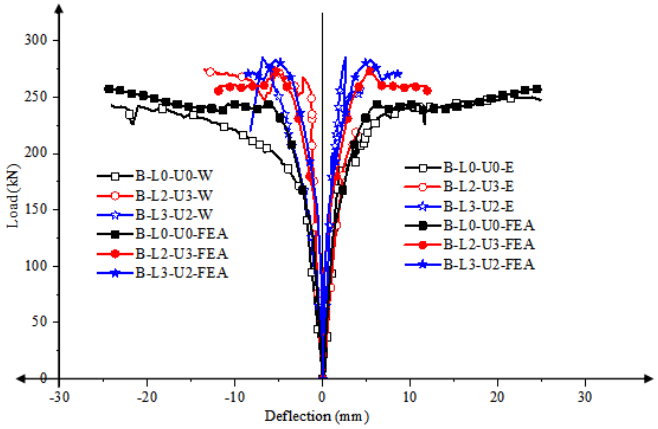

(b) Comparison of load-deflection curves of the specimens B-L0-U0, B-L2-U3 and B-L3-U2

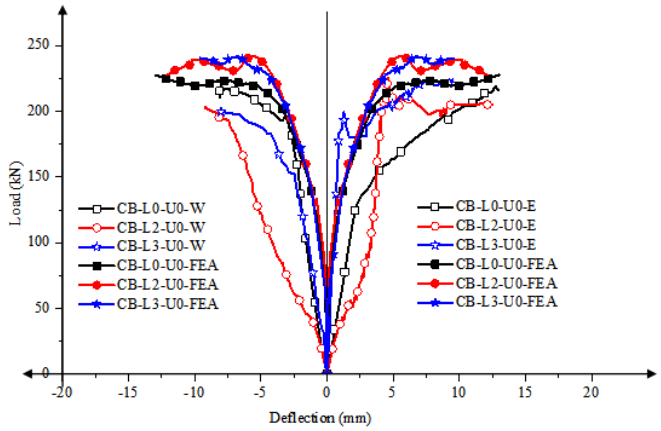

(c) Comparison of load-deflection curves of the specimens CB-L0-U0, CB-L2-U0 and CB-L3-U0

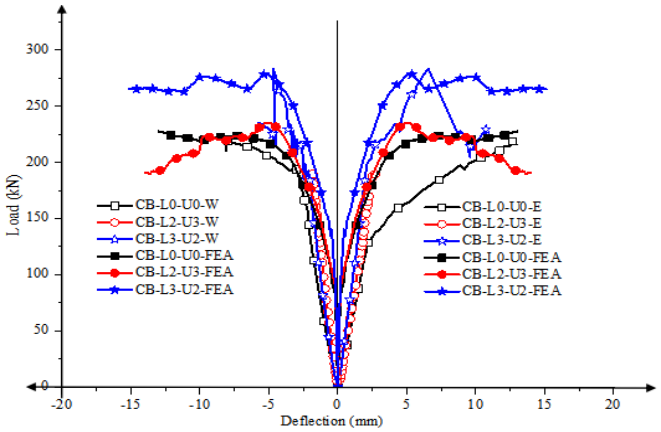

(d) Comparison of load-deflection curves of the specimens CB-L0-U0, CB-L2-U3 and CB-L3-U2

Figure 9. Comparison of load-deflection curves for RC continuous beams

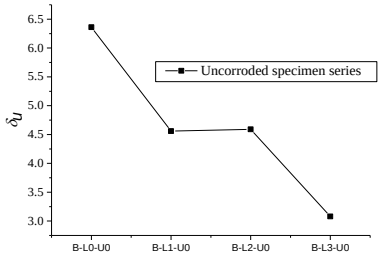

(a) Layer of CF mesh for uncorroded specimens

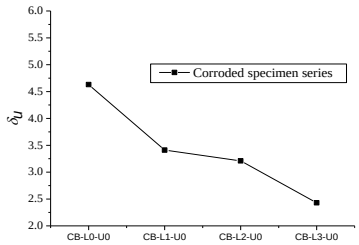

(b) Layer of CF mesh for corroded specimens

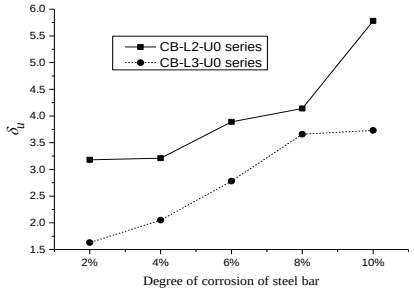

(c) Different degrees of corrosion of steel bar

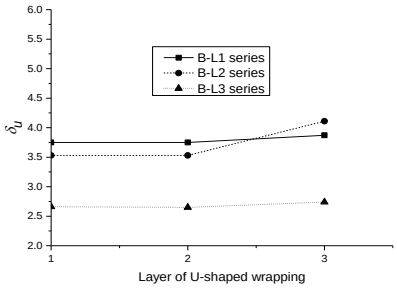

(d) Layer of complete wrapping

Figure 10. Comparison of ductility of specimens

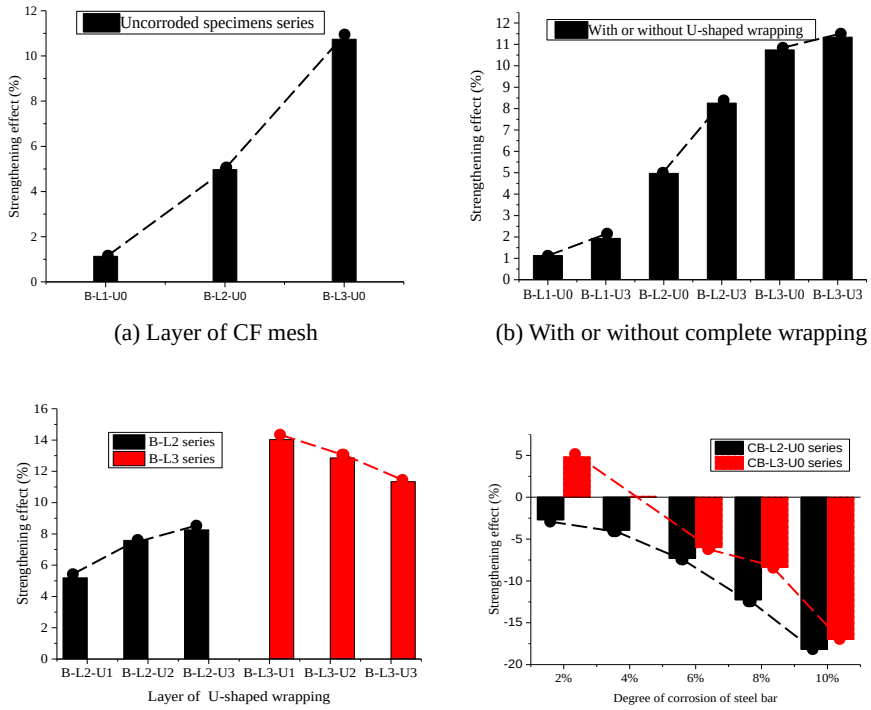

(a) Layer of CF mesh

(b) With or without complete wrapping

(c) Layer of complete wrapping

(d) Degree of corrosion of steel bar

Figure 11. Influence of a single factor in the layers of CF mesh, complete wrapping and degree of corrosion on the strengthening effect

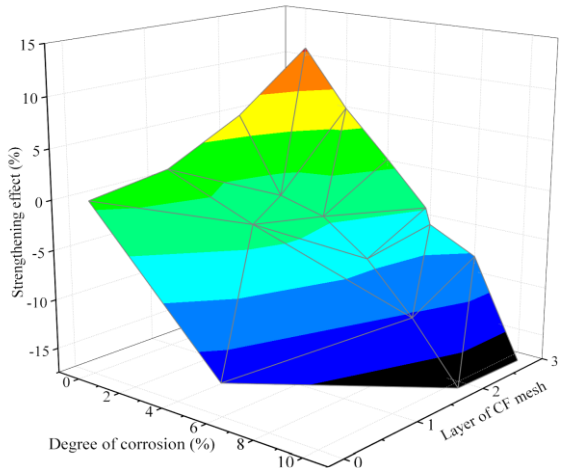

(a) Influence of the layer of CF mesh and degree of corrosion on the strengthening effect

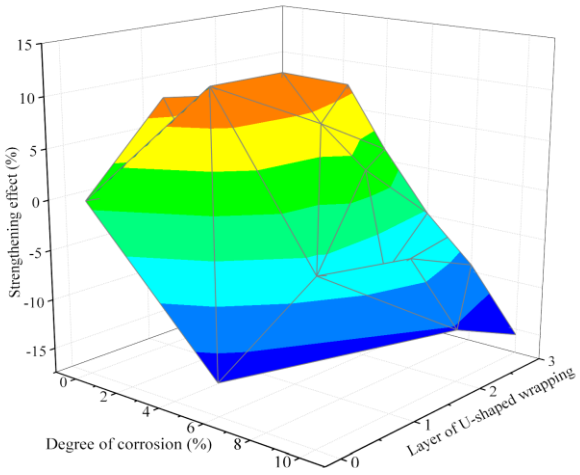

(b) Influence of the layer of complete wrapping and degree of corrosion on the strengthening effect

Figure 12. Coupling influence of layers of CF mesh and degree of corrosion, complete wrapping and degree of corrosion on the strengthening effect